

Coprecipitation of chromate with calcite: Batch experiments and X-ray absorption spectroscopy

Yuanzhi Tang ^{*}, Evert J. Elzinga ¹, Young Jae Lee ², Richard J. Reeder

*Department of Geosciences and Center for Environmental Molecular Sciences, State University of New York,
Stony Brook, NY 11794-2100, USA*

Received 24 May 2006; accepted in revised form 14 December 2006; available online 22 December 2006

Abstract

Batch experiments, combined with in situ spectroscopic methods, are used to examine the coprecipitation of Cr(VI) with calcite, including partitioning behavior, site-specific distribution of Cr on the surface of calcite single crystals, and local coordination of Cr(VI) in the calcite structure. It is found that the concentration of Cr incorporated in calcite increases with increasing Cr concentration in solution. The calculated apparent partition coefficient, K_d^* , is highest at low Cr solution concentration, and decreases to a constant value with increasing Cr solution concentration. DIC images of the (10 $\bar{1}$ 4) surface of calcite single crystals grown in the presence of CrO_4^{2-} exhibit well-defined growth hillocks composed of two pairs of symmetrically nonequivalent vicinal faces, denoted as + and –, which reflect the orientation of structurally nonequivalent growth steps. Micro-XRF mapping of the Cr distribution over a growth hillock shows preferential incorporation of Cr into the—steps, which is considered to result from differences in surface structure geometry. XANES spectra confirm that incorporated Cr is hexavalent, and no reduction of Cr(VI) in the X-ray beam was observed up to 2 days at room temperature. EXAFS fit results show the incorporated Cr(VI) has the expected first shell of 4 O at $\sim 1.64 \pm 0.01$ Å, consistent with CrO_4^{2-} . Best fit results show that the second shell is split with ~ 2.5 Ca at $\sim 3.33 \pm 0.05$ and ~ 2.2 Ca at $\sim 3.55 \pm 0.05$ Å, which confirms the incorporation of chromate into calcite. Consideration of possible local coordination indicates that significant distortion or disruption is required to accommodate CrO_4^{2-} in the calcite structure.

© 2006 Elsevier Inc. All rights reserved.

1. INTRODUCTION

Known as one of the most significant anthropogenic metal contaminants, Cr has been introduced into soils and water bodies as a result of its widespread use in industrial applications, such as tanning, metallurgy, plating, and as an anti-corrosion agent. The toxicity and transport behavior of Cr depend strongly on its valence. The most stable oxidation states in the environment are hexavalent

and trivalent (Patterson et al., 1997). Cr(VI) exists primarily in the form of HCrO_4^- (bichromate) and CrO_4^{2-} (chromate), which are strong oxidants that can cause kidney tubule necrosis and, by inhalation, lung cancer (cf. Beliles, 1979). Cr(VI) compounds are typically soluble in groundwater, and thus mobile and bioaccessible (Scott, 1994). Where intermediate to low redox potentials exist, Cr(VI) can be reduced to Cr(III) (Palmer and Wittbrodt, 1991), which usually forms insoluble oxides and oxyhydroxides that are less bioaccessible (Weckhuysen et al., 1996). Cr(III), except in large amounts, is considered an essential nutrient rather than a health risk (e.g., Beliles, 1979; Szulczewski et al., 1997).

To understand the transport behavior of Cr in soil and groundwater systems, knowledge of the Cr oxidation state and the mode(s) of Cr reaction with soil and sediment minerals is needed. Previous studies indicate that Cr(VI)

^{*} Corresponding author. Fax: +1 631 632 8240.

E-mail address: yuatang@ic.sunysb.edu (Y. Tang).

¹ Present address: Institute of Biogeochemistry and Pollutant Dynamics, Department of Environmental Sciences, ETH Zurich, Switzerland.

² Present address: Department of Earth and Environmental Sciences, Korea University, Seoul 136-701, Republic of Korea.

can react with iron sulfide, silicates and many other hydrous inorganic oxides such as Fe, Mn, Al oxides (e.g., Scott, 1994; Fendorf, 1995; Weckhuysen et al., 1996; Patterson et al., 1997; Peterson et al., 1997; Kendelewicz et al., 1999; Wei et al., 2002). For example, Patterson et al. (1997) found that amorphous iron sulfide minerals, such as mackinawite (FeS_{1-x}), have the potential to reduce large quantities of Cr(VI) and, in the process, form very stable $[\text{Cr,Fe}](\text{OH})_3$ solids. Wei et al. (2002) studied the thermal stabilization of Cr(VI) in kaolin by heating Cr(VI)-sorbed kaolin and used a leaching procedure to determine the percentage of mobile chromium from all heated samples. They found that at 500, 900, and 1100 °C hydrated Cr(VI) transformed to Cr_2O_3 , which is less toxic and more leach-resistant due to its low solubility.

Most of these studies addressed the reduction from Cr(VI) to Cr(III), which typically reduces Cr solubility and mobility. However, if reduction is not possible, Cr(VI) tends to be only marginally particle reactive, since it commonly forms only weakly held adsorption complexes on most mineral surfaces. Several studies have concluded that CrO_4^{2-} sorbs to oxide surfaces predominantly as outer-sphere complexes (e.g., Zachara et al., 2004) or weak inner-sphere complexes (e.g., Fendorf et al., 1997), which are susceptible to competitive sorption from other naturally occurring dissolved organic and inorganic ligands (e.g., Zachara et al., 1989; Garman et al., 2004). This allows Cr(VI) to remain highly mobile in soil water and ground water systems when adsorption is the predominant mode of Cr(VI) sequestration. Coprecipitation of Cr(VI), i.e., the incorporation of chromate into mineral structures, may be an effective alternative means of limiting the mobility of chromate.

Few studies have addressed the interaction of Cr with calcium carbonate minerals, despite the widespread occurrence of calcite in low-temperature aqueous environments. For instance, at the Hanford Site, where Cr(VI) is a significant ground water contaminant (Zachara et al., 2004), calcite occurs locally in subsurface sediments and may be locally associated with contaminant plumes. Garcia-Sánchez and Álvarez-Ayuso (2002) studied the sorption of Cr(III) onto calcite in a continuous flow system and found that the sorption process can be described by a Langmuir model, with Cr(III) precipitating on calcite as an oxide hydrocarbonate coating. We are not aware of any previous studies of the interaction between Cr(VI) and calcite. In settings where carbonate minerals are forming, it is important to know if interaction of Cr with calcium carbonate could be important for influencing Cr mobility.

The structure of calcite is based on corner sharing of triangular CO_3 groups with CaO_6 octahedra. The corner sharing makes the calcite structure very flexible and able to accommodate different substituent ions. Much work has been done on the coprecipitation of foreign ions with calcite. Morse and Bender (1990) examined the complexities associated with experimental coprecipitation studies and pointed out that such observed partitioning behavior does not reflect equilibrium and emphasized the need to consider kinetic factors affecting foreign ion partitioning between calcite and aqueous solutions. Factors such as overall growth rate (Lorence, 1981; Mucci and Morse, 1983; Pingi-

torre and Eastman, 1986) and the activities of other foreign ions (Pingitore and Eastman, 1986) are known to influence the partition behavior of trace and minor elements into calcite.

In recent years, it has been noted that path-dependent aspects, especially factors related to growth mechanism, are important in controlling trace ion incorporation during crystal growth. In the case of calcite, the most commonly occurring surface during single crystal growth, $\{10\bar{1}4\}$, exhibits polygonized growth hillocks composed of four vicinal faces, which indicates that growth occurs by the spiral mechanism. The four vicinal faces are defined by the orientation of the growth steps composing them and the direction of their advance during growth. They can be divided into two pairs of steps commonly denoted as “+” and “-” (Paquette and Reeder, 1990, 1995; Staudt et al., 1994; Reeder, 1996). The + steps include $[\bar{4}41]_+$ and $[48\bar{1}]_+$ steps, which are structurally equivalent. The - steps include $[441]_-$ and $[48\bar{1}]_-$ steps, which are also structurally equivalent. But + steps and - steps are structurally nonequivalent. The geometry and surface symmetry of these hillocks have been described in detail elsewhere (Paquette and Reeder, 1990, 1995; Dove and Hochella, 1993; Gratz et al., 1993; Staudt et al., 1994; Reeder, 1996; Teng et al., 1998). These nonequivalent steps allow for the possibility that cations and anions are incorporated differentially into structurally distinct steps during spiral growth. An understanding of the factors that influence such differential incorporation will provide the basis for mechanistic models of element interactions at mineral surfaces.

Previous studies have shown that divalent metal ions, e.g., Mn^{2+} , Co^{2+} , Zn^{2+} , Sr^{2+} , Ba^{2+} and Cd^{2+} (Reeder, 1996), and structurally incompatible anions such as SeO_4^{2-} , SO_4^{2-} , and $\text{B}(\text{OH})_4^-$ (Staudt et al., 1994; Hemming et al., 1998) exhibit different incorporation behaviors on the calcite $(10\bar{1}4)$ surface during crystal growth. Sr^{2+} , Pb^{2+} , Ba^{2+} , Mg^{2+} , Mn^{2+} , Co^{2+} , Cd^{2+} , Cu^{2+} , and Zn^{2+} have been shown to incorporate at Ca surface sites within different steps (Paquette and Reeder, 1995; Reeder, 1996; Temmam et al., 2000; Elzinga and Reeder, 2002). Elzinga and Reeder (2002) proposed that for the divalent metals considered the key factor determining the incorporation preference for different growth steps on the calcite $(10\bar{1}4)$ surface is the geometry of the adsorption complex.

Differential incorporation between nonequivalent steps has also been observed for anions. However, less is known about the mode of incorporation of structurally incompatible complex anions in the calcite structure. Observations have shown that SeO_4^{2-} , SO_4^{2-} , $\text{B}(\text{OH})_4^-$, and AsO_4^{3-} exhibit distinct preferences for incorporation at different vicinal faces (Reeder et al., 1994; Staudt et al., 1994; Hemming et al., 1998; Alexandratos, 2004). However, unlike for the cations, there have been no satisfactory explanations that account for the differential partitioning behavior of these oxyanions.

In this study, the macroscopic and microscopic partitioning behaviors of hexavalent Cr (CrO_4^{2-}) into calcite during crystal growth were studied. Batch uptake experiments were undertaken to provide macroscopic information on coprecipitation processes and partitioning

behavior of Cr(VI) between solid and solution. Microscopic and spectroscopic methods were used to examine the differential incorporation of Cr on the $(10\bar{1}4)$ growth surface of calcite single crystals. X-ray absorption spectroscopy was conducted in situ to characterize the oxidation state and local structure of incorporated Cr in calcite. The results provide new insight to Cr(VI) interactions with calcite, and a quantitative basis for evaluating the fate of Cr(VI) in environments where calcite crystallization is possible.

2. EXPERIMENTAL METHODS

2.1. Coprecipitation procedures

Two different experimental methods were used for Cr(VI) coprecipitation with calcite: a constant-addition method (Method I) and a modified free-drift method (Method II). Method I followed the modified constant-addition technique described by Reeder et al. (2000), which was adapted from the methods of Zhong and Mucci (1992) and Tesoriero and Pankow (1996). A stirred reaction vessel containing a CaCl_2 and NaHCO_3 solution was bubbled continuously with water-saturated air. NaCl was added initially to provide a background ionic strength of 0.1 M. An amount of 0.5 g calcite (Alfa Aesar, reagent grade, 5 μm particle size), which had been equilibrated with deionized water for over 2 weeks, was added as nucleation seeds. CaCl_2 and Na_2CO_3 solutions were pumped through separate syringes into the reaction vessel at a constant rate. K_2CrO_4 was added to the solution at the beginning of the experiment, which caused the solution pH to increase slightly. The initial concentration of Cr in the reaction vessel varied from 1 to 62.5 mM. Initial pH was adjusted to 7.9 ± 0.2 by addition of hydrochloric acid. The total reaction time for each experiment was 7–8 h. The solution pH increased initially and reached a constant value of 8.25 ± 0.1 within 4–5 h. Total CO_2 content in the solution was measured using the procedure described by Hall and Aller (1992) and, along with pH, was used to assess when the system had reached a near steady-state with respect to calcite supersaturation. The amount of total dissolved CO_2 dropped initially and reached a constant value after approximately 5 h, corresponding to near steady-state conditions. Total solution volume increased less than 20% over the duration of the experiments. As expected, the chromate concentration in the solution generally decreased by less than 30% over the duration of an experiment; in one case, however, the chromate concentration decreased by 50% after the reaction reached near steady-state conditions. The saturation index values (expressed as $\log(IAP/K_{\text{eq}})$) with respect to pure calcite were between 0.8 and 1.3, as calculated using the program PHREEQC (Parkhurst and Appelo, 1999). This coprecipitation method produced a chromate-containing calcite overgrowth on the pure calcite seeds. The final calcite powder was collected by vacuum filtration, washed multiple times with deionized water, and dried in an oven at 50 °C. X-ray diffraction (XRD) indicated there were no other phases than calcite, although we cannot rule out formation of a trace impurity phase. A portion of the final solid was weighed and dissolved in nitric acid,

and the Cr concentration was measured by direct coupled plasma (DCP) spectrophotometry. Aliquots of solution from the reaction vessel were collected periodically, and the Ca and Cr concentrations were also measured by DCP. These concentration data, combined with the Cr concentration in the solid, were used to calculate the Cr concentration in the overgrowth layer on the calcite seeds.

Method II is based on the modified free-drift method of Gruzensky (1967) and described in detail by Paquette and Reeder (1995) and Reeder (1996). A reaction vessel containing a CaCl_2 – NH_4Cl solution is sealed at room temperature with headspace in contact with a reservoir of solid ammonium carbonate. Decomposition of the ammonium carbonate provides NH_3 and CO_2 gases. The CO_2 yields CO_3^{2-} and HCO_3^- , which react with Ca^{2+} to precipitate CaCO_3 . The initial pH is 4.7–5, and pH increases as a result of the hydrolysis of $\text{NH}_3(\text{g})$. Calcite nucleation occurs on the bottom and walls of the vessel within 4–6 days, after which the pH remains nearly constant (7.6–7.8) as the calcite crystals increase in size. K_2CrO_4 was added after the solution pH stabilized, giving the solution a yellow color. Coprecipitation was allowed to occur up to 1 week after the addition of chromate. The initial Cr concentrations varied from 0.5 to 60 mM. Total CO_2 content in the solution was measured by the same procedure used in Method I. The saturation index values for calcite were in the range of 1.1–1.7, as calculated using PHREEQC. However, these values should be viewed with caution because of the limitations of the activity coefficient models at the high ionic strength (~ 2 M) of these solutions. Calcite single crystals were removed from the glass vessel, rinsed repeatedly with deionized water, and dried in air at ambient temperature. The resulting calcite crystals were clear, with some exhibiting a yellowish tint depending on the initial Cr concentration. Examination under the microscope showed them to be dominated by the common $\{10\bar{1}4\}$ growth form, corresponding to the perfect cleavage. Portions of the single crystals were ground to fine powder for X-ray absorption spectroscopy (XANES and EXAFS). Other single crystals were mounted and sectioned for differential interference contrast (DIC) imaging and synchrotron micro-X-ray fluorescence (μ -XRF) mapping described below.

2.2. Differential interference contrast (DIC) surface imaging and synchrotron micro-X-ray fluorescence (μ -XRF) mapping

Cr(VI)-doped calcite single crystals that exhibited a single spiral growth hillock on the $(10\bar{1}4)$ growth surface were selected for DIC and μ -XRF study. Crystals (200–400 μm in size) were ground and polished from the back, parallel to the face of interest, to a thickness of 50–60 μm , and mounted using EPOTEK 301 epoxy onto ultra-high-purity silica glass disks. The $(10\bar{1}4)$ growth surface is parallel to the disk and facing up, allowing DIC and μ -XRF analysis over the entire as-grown face.

DIC microscopy can display subtle deviations from a perfectly flat surface as different colors or shades of gray. It allows imaging of surface microtopographic features having vertical heights of approximately 20 Å or greater. With this resolution, individual monolayer steps, 3 Å on $(10\bar{1}4)$

faces, cannot be resolved. DIC microscopy showed polygonized growth spirals on the (10 $\bar{1}$ 4) face, which confirmed that the surface growth occurred by the spiral mechanism. Based on previous work, the incorporation of chromate is expected to be dominantly at the kink sites within steps on the (10 $\bar{1}$ 4) surface.

The concentration and spatial distribution of Cr were determined on the (10 $\bar{1}$ 4) surface sections of individual calcite crystals using μ -XRF at beamline X26A of the National Synchrotron Light Source (NSLS) at Brookhaven National Laboratory, Upton, New York, USA. The sample was positioned at 45° to the X-ray beam. A monochromatic X-ray beam was focused to a 6 \times 10 μ m spot. The X-ray fluorescence signal was detected by a Si(Li) detector. Area mapping was done over the entire (10 $\bar{1}$ 4) face with a step size of 10 μ m and dwell time of 10 s per pixel, which showed the Cr distribution within the new surface region on this face. Spot analyses were taken at representative locations on different vicinal faces with an acquisition time of 300 s. Absolute Cr concentrations were determined by standardless analysis, with instrumental parameters determined using a standard anorthite glass. Estimated relative errors of the concentrations are approximately 1%. A description of the analytical procedure was given by Lu et al. (1989).

2.3. X-ray absorption near-edge structure (XANES) and extended X-ray absorption fine structure (EXAFS) spectroscopy

XANES and EXAFS spectra of a Cr(VI)-containing calcite and Cr reference compounds were collected at beamline X11A and X11B of the National Synchrotron Light Source (NSLS; Brookhaven National Laboratory, Upton, NY) and at the bending-magnet beamlines at sector 12 (operated by BESSRC) and 20 (operated by PNC-CAT) of the Advanced Photon Source (APS; Argonne National Laboratory, Argonne, IL). The X-ray absorption spectroscopy (XAS) data of the reference materials (CaCrO₄, Cr₂O₃, and aqueous K₂CrO₄) were collected at the NSLS. For CaCrO₄ and Cr₂O₃, scans were taken at room temperature in transmission mode with gas-filled ionization chambers to monitor the X-ray intensities of the incident and transmitted beams. The gas mixtures in the ionization chambers were selected to absorb 20% of the incident and 80% of the transmitted intensities. For aqueous K₂CrO₄ (0.1 M, pH 12), spectra were taken in fluorescence mode with a Lytle detector positioned at 90° to the beam. Data were collected at the Cr K-edge (~5.989 keV) using a pair of Si(111) monochromator crystals. The monochromator was detuned by 30–35% for harmonic rejection. For energy calibration, the peak of the first derivative for spectra of a 5- μ m-thick Cr metal foil was positioned at 5.989 keV. The resolution of the monochromator at the Cr K-edge is approximately 1 eV.

The Cr(VI)-containing calcite sample selected for XAS (sample C25) contained an average Cr concentration of ~360 ppm; it was grown using the constant-addition method (Method I) at a pumping rate of 300 μ L/min and initial Cr solution concentration of 60 mM. The powdered sample was mounted in a Lucite sample holder covered with poly-

propylene film and positioned at 45° to the incident beam. An initial set of spectra (multiple scans) were collected at the APS sector 12 beamline at room temperature in fluorescence mode using a Canberra 13-element solid-state Ge detector positioned at 90° to the beam. The beam was used in a defocused mode to give a spot size of 1 \times 2 mm. A pair of Si(111) crystals was used for the monochromator, with one crystal detuned by 35%. A subsequent set of spectra were collected at the sector 20 beamline, where the beam size was 9 \times 1.3 mm. A pair of Si(111) crystals was used for the monochromator. A pair of Kirkpatrick-Baez mirrors, combined with crystal detuning of 10%, provided a high level of harmonic rejection. Data was collected in fluorescence mode with a Canberra 13-element solid-state Ge detector.

Data processing was performed with the EXAFS data analysis program WinXAS (Ressler, 1997). Spectra were averaged after energy calibration. The μ_0 fitting used a cubic spline. The $\chi(k)$ function was Fourier transformed using k^3 weighting, and all fitting was done in R -space. Theoretical backscattering paths were calculated using FEFF7 (Zabinsky et al., 1995) with CaCrO₄ as a model structure. A single threshold energy value (ΔE_0) was allowed to vary during fitting. The amplitude reduction factor, S_0^2 , was determined from fitting of the model compounds and was fixed at $S_0^2 = 0.9$ for the unknown sample. No constraints were placed on fitting parameters for the first-neighboring oxygen shells. Debye–Waller factors were fixed at 0.007 Å^2 for second and higher shells. This value is within the typical range (0.005–0.015 Å^2) of Debye–Waller factors for higher shells. Errors for the fitting parameters are estimated from fits of the reference materials CaCrO₄ and aqueous K₂CrO₄. Error estimates are ± 0.01 Å for the R value of the first shell and ± 0.05 Å for higher distance shells. For coordination number, which is correlated to the Debye–Waller factor, the estimated errors are $\pm 20\%$ for the first oxygen shell and $\pm 40\%$ for shells at higher distance. Estimated errors for the Debye–Waller factors are ± 0.001 Å^2 for the first shell and ± 0.005 Å^2 for higher shells.

3. RESULTS

3.1. Aqueous speciation

The aqueous speciation of Cr(VI) in the growth solution for the constant-addition method (Method I) was calculated using the program PHREEQC (Parkhurst and Appelo, 1999) with the MINTQA2 database (Allison et al., 1990). Activity coefficients of aqueous species are defined with the Davies equation or the extended Debye–Hückel equation. Solution concentrations used for the calculation correspond to the near steady-state solution conditions at pH 8.2, with Cr, Ca, and total CO₂ concentrations of 60, 5, and 1.8 mM, respectively. The speciation of Cr expressed as percentages is: CrO₄²⁻ 99.3%, HCrO₄⁻ 0.68%, Cr₂O₇²⁻ 0.02%. Thus, at the experimental pH 8.2 almost all of the Cr exists as CrO₄²⁻. For all the experiments carried out by this method, saturation indexes were in the range 0.8–1.3 with respect to calcite, and below zero for any other phases, indicating no other phases were oversaturated.

Because of the high ionic strength needed in Method II (~ 2 M), it is not possible to calculate a reliable speciation of Cr. Neither the Davies equation nor the extended Debye–Hückel equation provides reliable activity coefficients at this high ionic strength. Since Pitzer parameters for Cr interactions were not found, we calculated the activity coefficients using the Davies equation. Solution concentrations used were those of the near steady-state solution conditions: pH 7.6, and Cr, Ca, and total CO_2 concentrations of 60, 25, and 7 mM, respectively. The Cr speciation expressed as percentages is: CrO_4^{2-} 98.2%, HCrO_4^- 1.45%, $\text{Cr}_2\text{O}_7^{2-}$ 0.17%. Although these results should be viewed with much caution, they do suggest that CrO_4^{2-} is likely to be the dominant species in the Method II experimental solution. The estimated saturation index, $\log(\text{IAP}/K_{\text{eq}})$, for calcite using method II is in the range 1.1–1.7.

3.2. Batch coprecipitation experiments

Fig. 1a shows the relationship between the Cr(VI) concentration in the overgrowth (in ppm) and in the final solution (in mM) for the constant-addition growth experiments. These results show that increasing the Cr concentration in solution results in a near-linear increase of Cr incorporation into calcite for the conditions studied. For this correlation

we used the Cr concentration in the final solution as this corresponds most closely to near steady-state conditions, which are attained after approximately 5 h and assessed on the basis of periodic monitoring of solution pH, and Ca, Cr, total CO_2 concentrations in solution.

The partitioning of chromate between growing calcite and the parent solution can be expressed by the equation (cf. McIntire, 1963; Busenberg and Plummer, 1985)

$$K_d = [\text{CrO}_4^{2-}/\text{CO}_3^{2-}]_{\text{solid}}/[\text{CrO}_4^{2-}/\text{CO}_3^{2-}]_{\text{solution}}, \quad (1)$$

where brackets indicate chromate and carbonate concentrations in solid and solution. As written, this empirical K_d expression implies that CrO_4^{2-} substitutes for a CO_3 group in the structure. Such substitutions for carbonate have been studied for SO_4^{2-} , SeO_4^{2-} (Staudt et al., 1994), and $\text{BO}_3^{3-}/\text{B}(\text{OH})_4^-$ (Sen et al., 1994; Hemming et al., 1995), and we consider this aspect for CrO_4^{2-} elsewhere in this paper. This K_d expression can be applied to specifically consider the aqueous CrO_4^{2-} and CO_3^{2-} species, rather than total Cr and total CO_3 in solution. For Cr, there is little difference, however, as CrO_4^{2-} accounts for >98% of the total dissolved Cr, providing that no reduction to Cr(III) occurs. At the pH of our experiments, however, $[\text{CO}_3^{2-}]$ is only a small fraction of the total dissolved CO_2 in the solution, the greatest portion occurring as HCO_3^- . Eq. (1) can be

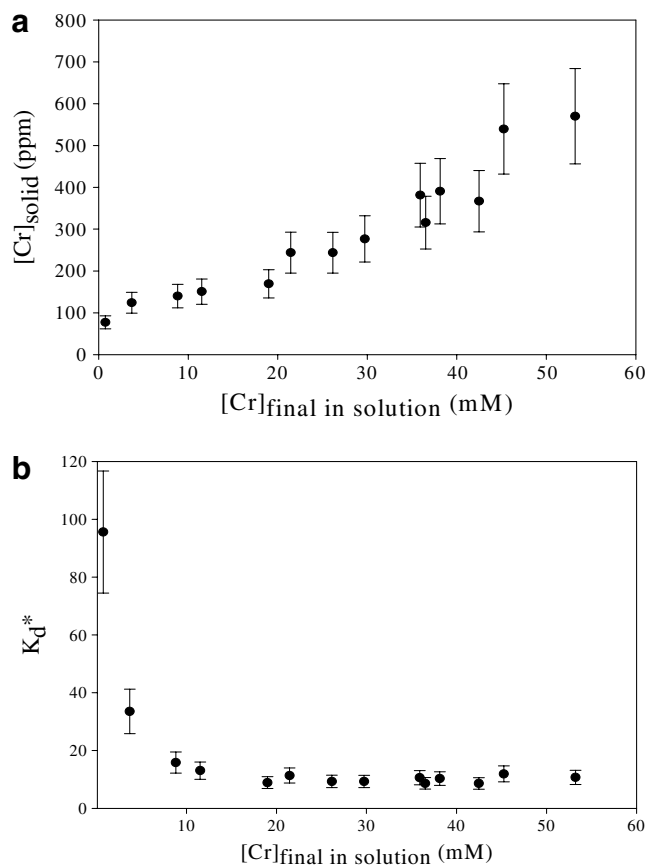


Fig. 1. (a) Cr in calcite overgrowth as a function of the Cr concentration in the final near steady-state solution. Error bars reflect the instrumental errors of the DCP and estimated errors from dilution; (b) plot showing apparent partition coefficient values, K_d^* , as a function of Cr concentration in the final solution.

rewritten using HCO_3^- , which is the dominant carbonate species in our solution. Hemming et al. (1995) used an alternate approach for quantifying borate coprecipitation with calcite, by accounting for the carbonate species in both the solid and the solution by a parameter C . This allows Eq. (1) to be simplified to

$$K_d = [\text{Cr}]_{\text{solid}} / [\text{Cr}]_{\text{solution}} \times C, \quad (2)$$

where $[\text{Cr}]_{\text{solid}}$ is the Cr concentration in the overgrowth (in ppm) and $[\text{Cr}]_{\text{solution}}$ is the total Cr concentration in the solution (in mM). Inasmuch as all the experimental solutions in Method 1 were essentially identical except for the Cr concentration in the solution and the overgrowth, C is essentially a constant and need not be shown. Thus Eq. (2) can be further simplified to

$$K_d^* = [\text{Cr}]_{\text{solid}} / [\text{Cr}]_{\text{solution}}, \quad (3)$$

where K_d^* represents an apparent partition coefficient taking into consideration the factors represented by C , and $[\text{Cr}]_{\text{solid}}$ and $[\text{Cr}]_{\text{solution}}$ are the Cr concentration in the overgrowth (in ppm) and the total Cr concentration in the solution (in mM), respectively. K_d^* values cannot be directly

compared with partitioning results obtained in other studies in which different solution conditions were used. However, we can use these values to compare relative partitioning behavior in this study.

The apparent partition coefficients are plotted as a function of Cr concentration in the final solution in Fig. 1b. It can be seen that for $[\text{Cr}]_{\text{solution}} > 10$ mM, K_d^* has a nearly constant value of ~ 10 . As $[\text{Cr}]_{\text{solution}}$ decreases below 10 mM, K_d^* increases, reaching a maximum observed value of ~ 95 for $[\text{Cr}]_{\text{solution}} = 0.75$ mM.

3.3. DIC microscopy and μ -XRF mapping of Cr distribution on calcite $(10\bar{1}4)$ growth faces

Differential interference contrast (DIC) microscopy revealed the growth microtopography on the $(10\bar{1}4)$ faces of the calcite single crystals. Fig. 2a is a DIC micrograph of a representative $(10\bar{1}4)$ surface, which exhibits a single polygonized growth hillock composed of four vicinal faces. Similar growth hillocks were observed on crystals grown with different Cr solution concentrations. The geometry and surface symmetry of these hillocks have been described

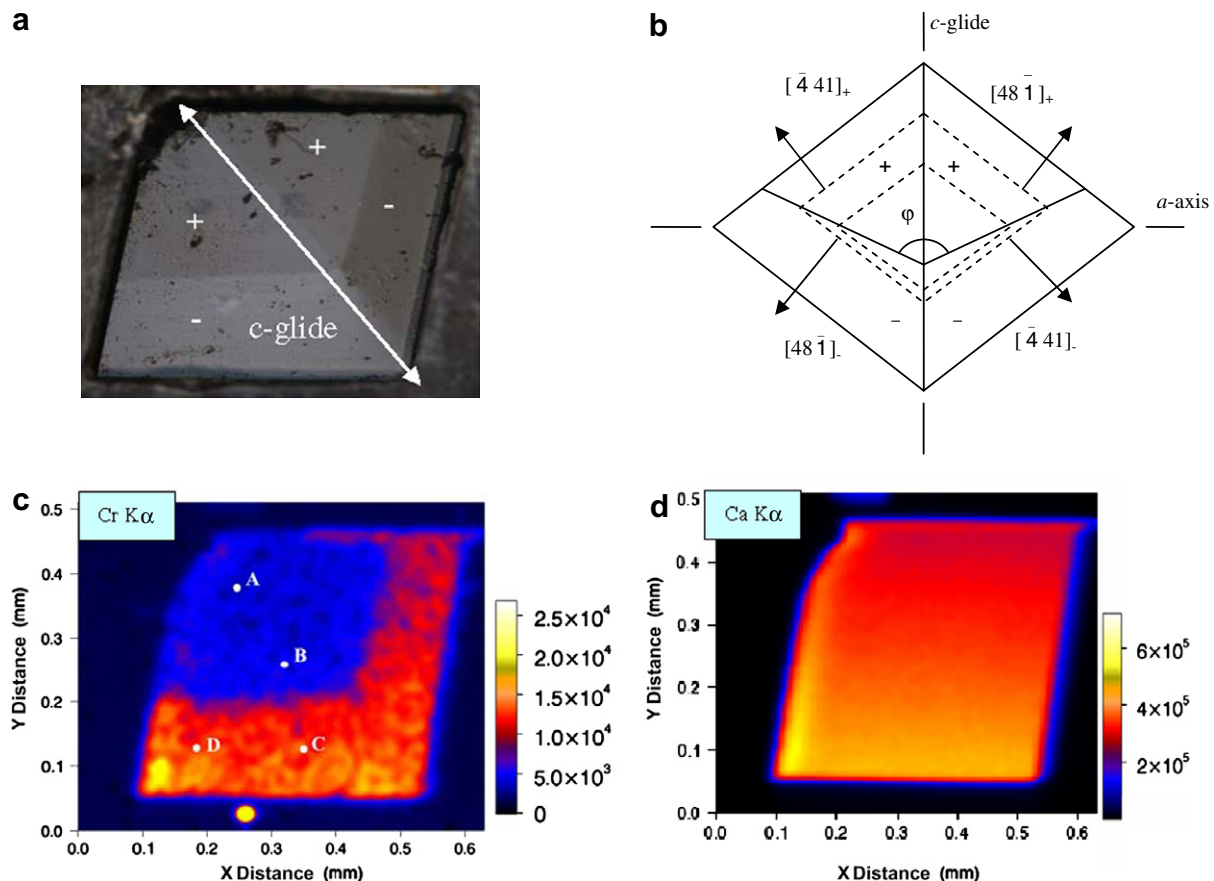


Fig. 2. (a) DIC image showing a $(10\bar{1}4)$ growth surface of a Cr-doped calcite single crystal (Method II). Different shading patterns represent nonequivalent vicinal faces resulting from spiral growth. (b) Schematic diagram showing the geometry of a single polygonized growth hillock on the calcite $(10\bar{1}4)$ surface. Dashed lines show orientations of growth steps in vicinal faces labeled + and -. The trace of the c-glide symmetry element is shown. (c) and (d) μ -XRF maps showing Cr and Ca distributions on the same surface shown in (a). Cr K α and Ca K α counts are indicated by scale bars at right. Points A, B, C, and D show locations of spot analysis in different vicinal faces. Cr concentrations for A, B, C, and D are 89, 92, 267, and 263 ppm, respectively.

in detail (Paquette and Reeder, 1990; Staudt et al., 1994; Paquette and Reeder, 1995; Reeder, 1996), and atomic force microscopy studies have documented their growth activities (Dove and Hochella, 1993; Gratz et al., 1993; Teng et al., 1998). Fig. 2b shows a schematic diagram of the geometry of a single polygonized growth hillock. The $[441]_+$ and $[48\bar{1}]_+$ steps composing the “+” vicinals are symmetrically equivalent, and the $[441]_-$ and $[48\bar{1}]_-$ steps composing the “-” vicinals are equivalent. However, these two step pairs are not equivalent, which allows the possibility that cation and anion impurities are incorporated differently into these structurally distinct steps during growth.

The angle ϕ (Fig. 2b), defined by the edges separating adjacent pairs of nonequivalent vicinal faces, reflects the relative difference in velocity of monolayer growth steps moving in opposite directions. Gratz et al. (1993), Paquette and Reeder (1995), and Reeder (1996) studied the range of ϕ values and the associated step velocity differences. Teng et al. (2000) found that growth velocities of the “+” steps can be either higher, nearly equal to, or lower than the “-” steps at different supersaturations. When the different step velocities are equal, the angle ϕ should be $\sim 180^\circ$ (Reeder, 1996). The fact that ϕ is less than 180° under our experimental conditions indicates that the “+” steps have higher growth velocities than the “-” steps.

A μ -XRF elemental map showing the Cr distribution in a representative Cr-doped single crystal having a single growth hillock on the $(10\bar{1}4)$ face is shown in Fig. 2c. This crystal is grown with Cr solution concentration of 25 mM. Cr $K\alpha$ counts are shown on the accompanying bar scale. From the shading pattern it is clear that the distribution of Cr differs significantly between the + and - vicinal regions, whereas there is no difference between symmetrically equivalent vicinals. Spot analyses were obtained from four representative locations (indicated by letters A, B, C, and D in Fig. 2c), which yielded Cr concentrations of 89, 92, 267, and 263 ppm, respectively. These results confirm that Cr is preferentially incorporated into the - steps relative to the + steps during spiral growth. The corresponding μ -XRF map in Fig. 2d reveals a uniform Ca distribution in the same crystal as shown in Fig. 2c. The uniform shading also indicates that the thickness of the crystal section is uniform. For single crystals grown with Cr solution concentration of 60 mM, representative Cr concentrations in + and - vicinal regions are 225 and 620 ppm, respectively.

3.4. XANES analysis of Cr oxidation state

Inasmuch as XANES spectra for Cr(VI) and Cr(III) compounds are significantly different, we used this method to confirm the oxidation state of Cr incorporated into the calcite. A prominent pre-edge peak at ~ 5989 eV occurs when Cr is present as Cr(VI), due to the 1s to 3d electronic transition. This transition is allowed for noncentrosymmetric tetrahedral Cr(VI) molecules due to the mixing of Cr 3d and O 2p orbitals. The empty d-orbital ($3d^0$) of Cr(VI) increases the probability of this 1s to 3d transition, and enhances the pre-edge peak intensity. This transition is forbidden for Cr(III), which occurs almost exclusively in octahedral coordination and is centrosymmetric (Burns, 1993).

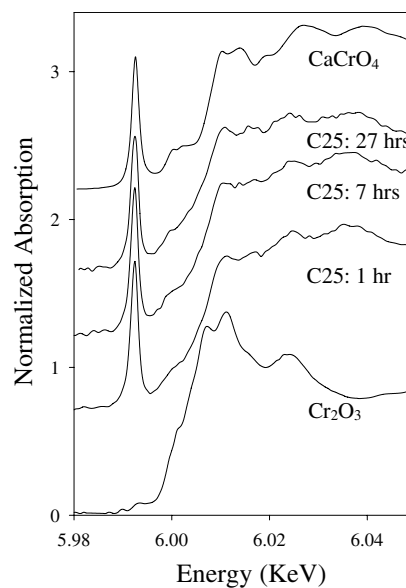


Fig. 3. XANES spectra of Cr_2O_3 , CaCrO_4 , and Cr-doped calcite sample C25. Spectra for C25 are shown after different durations of scanning at room temperature: after 27 h, after 7 h, and the average of the first four spectra.

In addition, the main edge position for Cr(III) is at lower energy than that of Cr(VI). When Cr(VI) appears in a compound that also contains Cr(III) the height of the pre-edge peak is diminished, and the main-edge shifted to lower energy (Patterson et al., 1997; Peterson et al., 1997; Wei et al., 2002; Zachara et al., 2004). In fact, the ratio of the pre-edge peak height and the normalized edge step has been used to estimate the percentages of Cr(VI) and Cr(III) in samples (e.g., Patterson et al., 1997; Peterson et al., 1997; Wei et al., 2002; Zachara et al., 2004).

Fig. 3 compares the XANES spectra of CaCrO_4 , Cr_2O_3 , and calcite sample C25, containing ~ 360 ppm Cr. CaCrO_4 and Cr_2O_3 are reference compounds for Cr in 6+ and 3+ oxidation states, respectively. The XANES spectrum of sample C25 shows a significant pre-edge peak at the same position (~ 5.991 keV) as that of CaCrO_4 . Also, the height of this pre-edge peak is similar to that for CaCrO_4 in normalized spectra. This indicates that almost all of the Cr in sample C25 exists as tetrahedrally coordinated Cr(VI). XANES spectra of the same sample taken after 7 and 27 h exposure to the X-ray beam show no decrease in the height of the pre-edge peak. This indicates that no observable reduction of Cr(VI) to Cr(III) occurred.

3.5. EXAFS analysis of Cr(VI) local structure in bulk calcite

Fig. 4(a and b) shows the k^3 -weighted, background-subtracted EXAFS data and corresponding Fourier transform magnitudes and imaginary components for Cr(VI)-doped calcite sample C25 and the reference compounds Cr_2O_3 , CaCrO_4 and aqueous K_2CrO_4 . Both raw data and fits are shown. It is evident that the EXAFS function for sample C25 shows no similarity to that of Cr_2O_3 , only slight similarity to that of CaCrO_4 , and is most similar to that of

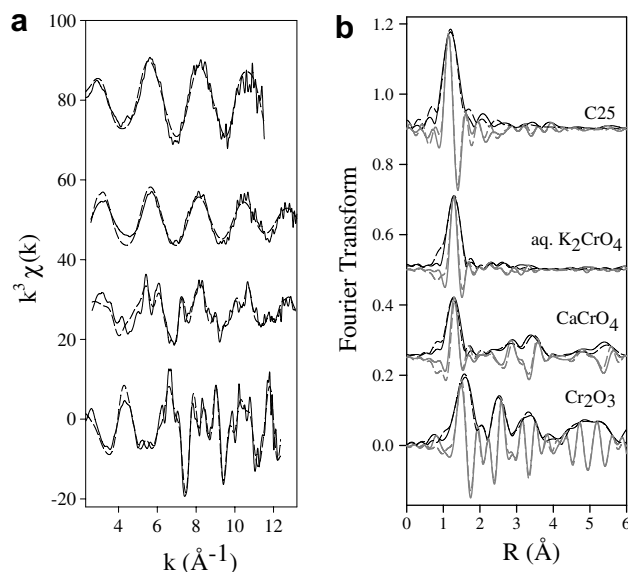


Fig. 4. (a) The k^3 -weighted, background-subtracted EXAFS data (solid lines) for Cr_2O_3 , CaCrO_4 , aqueous K_2CrO_4 , and sample C25, with best fit (dashed lines); (b) corresponding Fourier transform magnitudes and imaginary components (black and gray solid lines, respectively) and best fit in R -space (black and gray dashed lines).

aqueous K_2CrO_4 . Poor signal to noise in the Cr(VI)-doped calcite results from the low overall Cr concentration. A second EXAFS data set was obtained at a different beamline in an effort to improve upon the data quality, but only slightly better results were obtained. The k range is effectively limited to $\sim 11.6 \text{ \AA}^{-1}$. The Fourier transform magnitude for C25 shows a dominant low- R peak corresponding to an O first shell. Fitting of the first shell of the Cr(VI)-doped calcite indicates that Cr is surrounded by ~ 4 O atoms at a uniform distance of $\sim 1.64 \pm 0.01 \text{ \AA}$ (Table 1). This distance is slightly shorter than the Cr–O distance obtained from EXAFS fits of CaCrO_4 ($\sim 1.66 \text{ \AA}$) and aqueous

K_2CrO_4 ($\sim 1.68 \text{ \AA}$), but is consistent with the range of Cr–O distances for tetrahedral coordination of Cr(VI) (cf. Shannon, 1976). This distance is significantly shorter than Cr(III)–O distances for octahedral coordination ($\sim 1.99 \text{ \AA}$), as is evident in the Fourier transforms. The tetrahedral coordination of Cr in sample C25 is also indicated by the pre-edge peak in the XANES spectra. The small Debye–Waller factor of 0.001 also suggests little distortion within this oxygen shell.

The Fourier transform for the Cr(VI)-doped calcite exhibits several weak features at ~ 2.1 , 2.6, 3.5, and 4.0 \AA in the Fourier transform magnitude (not corrected for

Table 1

Cr K-edge EXAFS fit parameters for CaCrO_4 , Cr_2O_3 , and Cr-doped calcite sample C25

Shell	C.N.	R (\AA)	σ^2 (\AA^2)	Shell	C.N.	R (\AA)	σ^2 (\AA^2)
<i>Cr_2O_3</i>				<i>CaCrO_4</i>			
Cr–O	6 ^a	1.99	0.003	Cr–O	4 ^a	1.66 ^b	0.002
Cr–Cr	1 ^a	2.71	0.005	Cr–Ca	2 ^a	3.17 ^b	0.004
Cr–Cr	3 ^a	2.92	0.002	Cr–O	4 ^a	3.48 ^b	0.006
Cr–Cr	3 ^a	3.42	0.002	Cr–Cr	4 ^a	3.97 ^b	0.007
Cr–Cr	6 ^a	3.66	0.006	Cr–Ca	4 ^a	3.97 ^b	0.006
Cr–Cr	6 ^a	5.01	0.004	Cr–Ca	4 ^a	5.15 ^b	0.006
Cr–Cr	6 ^a	5.32	0.005	Cr–Cr	4 ^a	5.98 ^b	0.009
Cr–Cr	9 ^a	5.73	0.003	Cr–Ca	4 ^a	5.98 ^b	0.002
				Cr–Cr	8 ^a	6.04 ^b	0.004
<i>Aqueous K_2CrO_4</i>				<i>CrO_4^{2-}-doped calcite sample C25</i>			
Cr–O	4 ^a	1.68	0.004	Cr–O	4.6	1.64	0.001
MS (CrOOCr)	12 ^a	3.09	0.002	Cr–Ca	2.5	3.33	0.007 ^a
				Cr–Ca	2.2	3.55	0.007 ^a

Estimated errors for the first shells are $\pm 20\%$ for the coordination number, $\pm 0.01 \text{ \AA}$ for the R values, and $\pm 0.001 \text{ \AA}^2$ for the Debye–Waller factors; errors for the higher shells are $\pm 40\%$ for the coordination number, $\pm 0.05 \text{ \AA}$ for the R values, and $\pm 0.005 \text{ \AA}^2$ for the Debye–Waller factors.

^a Fixed.

^b Fixed, xyz lattice correlated.

phase shift). Several strategies were used to fit these longer correlations. On the basis of EXAFS studies of SeO_4^{2-} and AsO_4^{3-} incorporation into calcite (Reeder et al., 1994; Alexandratos, 2004) we expected to find that CrO_4^{2-} would substitute in the position occupied by CO_3^{2-} groups, which is defined by six Ca atoms forming an octahedron. Clearly some distortion or disruption of the local structure is required to accommodate the tetrahedral geometry in a nominally octahedral site. If the Cr atom of the CrO_4^{2-} unit were positioned in the center of this octahedral site, at the same position as a C atom, there would be a six equivalent Cr–Ca distances, which would correspond to a single shell in the Fourier transform. However, fits using a single Ca shell were unsatisfactory and failed to account for the several features in the Fourier transform at ~ 2.6 , 3.5 , and 4.0 Å in R -space. Therefore, we considered that, minimally, the CrO_4^{2-} unit had been forced to adopt an off-center position in the CO_3 site, or alternatively that the Ca atoms defining the carbonate site are displaced nonuniformly. Either case would result in two or more Cr–Ca distances. A fit using two Ca shells (~ 2.5 Ca atoms at 3.33 ± 0.05 Å and ~ 2.2 atoms at 3.55 ± 0.05 Å) resulted in the best agreement (Fig. 4). It is worth noting that the individual backscattering contributions from the two Ca shells at 3.33 and 3.55 Å are out of phase (Fig. 5), which could be at least partly responsible for the low amplitudes of these higher R features in the Fourier transform and give rise to large uncertainty of the fit parameters for these two shells.

We also considered the possibility that these higher R features could indicate Cr–Cr backscattering. It was possible to obtain a fit with ~ 2.3 Cr at ~ 3.30 Å and ~ 2.2 Cr at 3.51 Å. However, we do not consider structure models with these distances to be likely. According to Hoffmann et al. (2001), the Cr–Cr distance in dichromate is ~ 3.21 Å, which is shorter than our fit at ~ 3.30 Å. Moreover, our speciation calculation has shown that the dominant species in the solution is chromate, with dichromate being insignificant. We believe it would be unlikely to have two unlinked chromate tetrahedra sufficiently close to each other to yield Cr–Cr

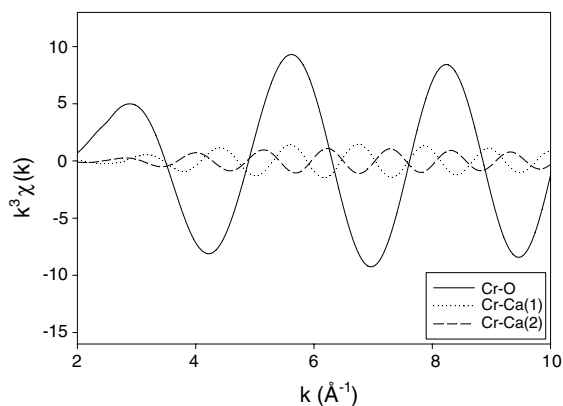


Fig. 5. Individual backscattering contributions from the O shell at distance of $R(\text{O}) = 1.64 \pm 0.01$ Å and two Ca shells at distances of $R(\text{Ca1}) = 3.33 \pm 0.05$ Å and $R(\text{Ca2}) = 3.55 \pm 0.05$ Å. Dotted and dashed lines represent the closer and further Ca shells, respectively.

distances of ~ 3.30 and 3.51 Å. Therefore we discount this possibility.

We were able to fit the ~ 2.1 Å feature satisfactorily by introducing either a third Ca shell at 2.2 ± 0.05 Å or an O shell at ~ 2.6 Å. However, we do not consider either structural model to be correct since a 2.2 Å Cr–Ca distance is too short to be physically realistic and we cannot explain a 2.6 Å Cr(VI)–O distance in addition to four 1.64 Å Cr(VI)–O distances. We were also able to force a fit of this peak with ~ 3 C at ~ 2.73 Å. This distance could only be explained, however, by corner sharing of an oxygen atom between CO_3 groups and a CrO_4 tetrahedron, for which the Cr–C distance would be between ~ 2.5 and 2.9 Å. However, the coordination number of 3 would suggest multiple corners are shared. This would only seem possible if multiple oxygen atoms are exchanged cooperatively. Inasmuch as both CrO_4 and CO_3 units are negatively charged, we consider this a very unlikely configuration.

Other workers have noted the importance of multiple-scattering contributions in chromate EXAFS spectra (e.g., Pandya, 1994; Hoffmann et al., 2001). We tried fits using the three MS paths of chromate ion as described by Hoffmann et al. (2001), including a 12-fold 3-leg path CrOOCr (MS1), a 4-fold collinear path CrOCrOCr (MS2), and a 12-fold path CrOCrOCr (MS3), which involves backscattering from two different oxygen atoms. This strategy did not yield improved fits (fits are not shown here). Furthermore, since the position and amplitude of this peak in the Fourier transform tend to change according to the EXAFS k range used, it is likely to be an artifact caused by the short k range.

We consider the feature at ~ 4.0 Å to be real because its position and amplitude are not affected by changing the EXAFS data range. We were able to fit the ~ 4 Å feature satisfactorily by introducing either a third Ca shell of ~ 2 Ca at 4.50 ± 0.05 Å or a Cr shell of ~ 1.9 Cr at $\sim 4.56 \pm 0.05$ Å (Fig. 4). The fit with ~ 2 Ca at $\sim 4.50 \pm 0.05$ Å is structurally more reasonable. In calcite, there are two second-neighbor Ca atoms around a central C atom at ~ 4.27 Å. If we consider substitution of a chromate tetrahedron in the CO_3 site, it is plausible that local distortion, which is probably significant, could account for a Ca shell at a longer distance ($\sim 4.50 \pm 0.05$ Å). If the fit with ~ 1.9 Cr at $\sim 4.56 \pm 0.05$ Å were correct, one possibility is to have two chromate ions substituting in neighboring CO_3 sites. In calcite, the shortest distance between two C atoms is ~ 4.05 Å and the O–O distance in a CO_3 group is ~ 2.22 Å. Given the larger size of a chromate tetrahedron, with $\langle \text{Cr–O} \rangle = \sim 1.64$ Å and $\langle \text{O–O} \rangle = \sim 2.67$ Å, the local structure would be greatly distorted to adapt neighboring chromate ions. Because of the great uncertainty associated with the limited data range and data quality, however, we cannot rule out either fit, or some other configuration. Furthermore, if any, or both of the shells are real, this might indicate multiple local environments of the incorporated chromate.

Despite the uncertainties in fit results obtained for higher shells, backscattering contributions are evident from Ca atoms, from at least two distances, 3.33 ± 0.05 and 3.55 ± 0.05 Å. This finding lends strong support to the

inference that CrO_4^{2-} occupies the carbonate position, albeit distorted, with second-neighbor Ca atoms. However, we cannot rule out the possible existence of multiple local environments.

4. DISCUSSION

4.1. Possible modes of CrO_4^{2-} incorporation in calcite

It has long been a dilemma how tetrahedral oxyanions can substitute in the calcite structure, which lacks a tetrahedral site. For divalent oxyanions, such as CrO_4^{2-} , charge balance would suggest substitution for the carbonate groups in calcite. However, the geometry of a tetrahedron is not compatible with the planar triangular carbonate group, and the O–O edge lengths differ significantly, with the O–O length being ~ 2.6 – 2.7 Å in CrO_4^{2-} and 2.22 Å in CO_3^{2-} . Hence large distortions or disruption of local structure would be required to accommodate such a substitution. Busenberg and Plummer (1985) speculated that SO_4^{2-} coprecipitation with calcite was accommodated by defect sites and correlated with coprecipitation of Na^+ . Our XANES and EXAFS results confirm that Cr occurs as CrO_4^{2-} , and the EXAFS results further show that ~ 5 – 6 Ca atoms occur as second-neighbors to Cr(VI) at distances of 3.3 – 3.5 Å, with two Ca shells likely at slightly different distances. This range of Cr–Ca distances is slightly greater than the C–Ca distance in calcite (3.21 Å), as would be expected for the larger size of CrO_4^{2-} compared to CO_3^{2-} . However, our inability to determine a unique structural model from these results limits further interpretation of the CrO_4^{2-} coordination in calcite.

Reeder et al. (1994) used EXAFS to examine the local structure of SeO_4^{2-} incorporated in calcite during crystal growth. They identified two second-neighbor Ca shells, with ~ 3 Ca atoms at ~ 3.17 Å and ~ 3 Ca atoms at ~ 3.49 Å, and proposed two potential coordination environments. Their so-called axial position has one face of the SeO_4 tetrahedron (three oxygen atoms) maintaining the same coordination as the carbonate group of calcite, with the Se atom and the fourth apical oxygen atom lying on the 3-fold axis of the carbonate octahedral site. The three Ca atoms surrounding the apical oxygen atom have different displacements than those three Ca atoms surrounding the three basal oxygen atoms, which give rise to a split Ca shell. The two Cr–Ca distances of $\sim 3.33 \pm 0.05$ and $\sim 3.55 \pm 0.05$ Å in our results (Table 1) fall in the range of displacement predicted by Reeder et al. (1994). Their second possible position, referred to as a nonaxial position, can be derived by rotating the SeO_4 tetrahedron 35° from the axial position around one basal O–O edge. The two oxygen atoms of this basal edge are close to four Ca atoms and must have different displacements relative to the two opposite oxygen atoms, which are in close proximity to two Ca atoms. Reeder et al. (1994) favored the nonaxial model because it would be expected to cause less distortion than the axial position. Either of these models could apply for CrO_4^{2-} , and we cannot distinguish, which, if either, is correct. Moreover, it is possible that the accommodation of CrO_4^{2-} requires involvement of another guest species,

such as H_2O . We note that Phillips et al. (2005) concluded that structural water was associated with the incorporation of citrate into calcite, presumably facilitating its coordination. Overall, and despite the uncertainties from the EXAFS results, we tentatively conclude that CrO_4^{2-} substitutes in carbonate positions in the calcite, but without a clear view of the mode of incorporation.

4.2. Site-selective incorporation of CrO_4^{2-} at the calcite surface

One of the more compelling arguments for believing that CrO_4^{2-} maintains some regular structural registry with the calcite lattice is the observation that this tetrahedral unit shows preferential incorporation at one set of surface steps as opposed to the other (Fig. 2). This indicates that the CrO_4^{2-} group is sensitive to subtle differences in surface coordination. Previous studies have shown that both divalent metals and structurally incompatible anions exhibit site-selective incorporation behavior on the calcite (10 $\bar{1}$ 4) surface during crystal growth. This differential partitioning behavior is considered to be constrained by site geometry and coordination preferences, and demonstrates path-dependent partitioning. Crystallographic and/or X-ray absorption spectroscopy studies indicate that divalent impurity cations substitute in Ca sites, whereas anions are accommodated at carbonate sites but not without local distortion (Reeder et al., 1994; Staudt et al., 1994; Paquette and Reeder, 1995; Reeder, 1996; Hemming et al., 1998; Elzinga and Reeder, 2002).

In this study, Cr(VI) is found to be preferentially incorporated into the $-$ steps of the calcite (10 $\bar{1}$ 4) surface during crystal growth. Speciation calculations indicate that (nonprotonated) CrO_4^{2-} is the dominant species in growth solutions. XANES and EXAFS results confirm that the incorporated Cr is hexavalent and in tetrahedral coordination with oxygen, as in CrO_4^{2-} .

Using a similar crystal growth method, Staudt et al. (1994) found that SeO_4^{2-} and SO_4^{2-} were preferentially incorporated into the $+$ steps of the (10 $\bar{1}$ 4) calcite surface. Staudt et al. (1994) proposed that differences in site geometries of nonequivalent kink sites are the controlling factors for differential incorporation of these anions (see Fig. 8 in Staudt et al., 1994). Vicinal faces composed of steps with more open and geometrically less constrained kink sites would allow greater SeO_4^{2-} and SO_4^{2-} incorporation, whereas vicinal faces containing more constrained kink sites would permit less SeO_4^{2-} and SO_4^{2-} incorporation.

The size of CrO_4^{2-} is similar to that of SeO_4^{2-} and SO_4^{2-} ($\langle \text{O–O} \rangle = \sim 2.6$ – 2.67 Å for SeO_4^{2-} , ~ 2.6 – 2.7 Å for CrO_4^{2-} , ~ 2.35 – 2.45 Å for SO_4^{2-} , and they have the same charge and tetrahedral geometry. If differential incorporation is controlled by the surface site geometry alone (cf. Staudt et al., 1994), one would expect that CrO_4^{2-} behaves as SeO_4^{2-} and SO_4^{2-} do, i.e., preferentially incorporating into the $+$ steps. However, we observed that CrO_4^{2-} favors the $-$ steps over the $+$ steps, which indicates that surface site geometry alone cannot explain the site-selective incorporation of tetrahedral oxyanions.

Boron oxyanions also show step-selective incorporation on the calcite ($10\bar{1}4$) surface during crystal growth, being preferentially incorporated into the $-$ steps (Hemming et al., 1998). The first-shell coordination of boron was shown to undergo changes during the incorporation process (Sen et al., 1994). Almost 90% of incorporated boron species in the calcite occur in trigonal coordination and 10% in tetrahedral coordination. It is possible that this $\sim 90:10$ ratio of trigonal to tetrahedral boron is not uniform between nonequivalent vicinal faces. However, it was not possible to determine the exact identity of the trigonally coordinated boron species (e.g., $\text{B}(\text{OH})_3^0$, BO_3^{3-} , etc.). Hemming et al. (1998) proposed that the coordination change of the boron species might be a controlling factor for the preferential incorporation behavior.

Boron oxyanion species and CrO_4^{2-} have the same step preference during incorporation, both preferring the $-$ steps. However, our XANES and EXAFS results showed that no coordination change of CrO_4^{2-} occurs during incorporation, nor was a change of oxidation state from Cr(VI) to Cr(III) observed. Thus structural constraints associated with a coordination change cannot be a controlling factor for the site-selective incorporation of CrO_4^{2-} into calcite.

Recent work by Alexandratos (2004) has shown that arsenate species are preferentially incorporated into the $-$ steps of the calcite ($10\bar{1}4$) surface during crystal growth. Speciation calculations for their experimental pH (7.6) showed HAsO_4^{2-} to be the dominant As species in the growth solution. Arsenic K-edge EXAFS results of As(V)-containing calcite confirmed tetrahedral coordination as expected. The size of the AsO_4 tetrahedron is similar to that of SeO_4 and SO_4 tetrahedra, with $\langle\text{O}-\text{O}\rangle \sim 2.67\text{--}2.82$ Å. Satisfactory explanations for the step-selective partitioning behavior of arsenate were not given. Even if it were assumed that HAsO_4^{2-} was directly taken up from solution into the calcite structure, it is not clear if the involved proton could have some influence on the behavior.

The size of the chromate tetrahedron is similar to that of arsenate. Neither undergoes a coordination change during incorporation, and both show the same preference for the $-$ steps on the calcite ($10\bar{1}4$) surface. $\text{CrO}_{4(\text{aq})}^{2-}$ is shown to be the dominant species in solution, but XANES and EXAFS spectra are not able to identify if a proton is associated with Cr(VI) in the calcite structure (e.g., HCrO_4^-). It is also noteworthy that arsenate adsorbs strongly onto calcite, whereas we infer that chromate adsorption is weak.

At present there is insufficient information to give a satisfactory explanation for the differential incorporation behaviors of the oxyanions discussed. However, the effects of surface-site differences and coordination geometry are believed to be important. One possible explanation considered by Hemming et al. (1998) involves the influence of differences in growth step velocities between nonequivalent steps on impurity incorporation. Several studies have demonstrated that K_d values for trace element incorporation between solid and fluid are dependent on growth rate (e.g., Lorence, 1981; Morse and Bender, 1990), with the general tendency being that K_d values for incompatible cations ($K_d < 1$) increase with increasing growth rate, while those with $K_d > 1$ decrease with increasing growth rate. Busen-

berg and Plummer (1985) reported that the K_d value for SO_4^{2-} incorporation into calcite increases with increasing growth rate, which is consistent with its incompatibility. One could argue that such a kinetic influence on coprecipitation also applies at the scale of growth steps, as these are the predominant sites for attachment during growth. Thus, where two steps advance at different velocities, as on the calcite ($10\bar{1}4$) surface, an incompatible impurity should exhibit greater incorporation at the faster moving step. Hemming et al. (1998) found the ratio of $+$ and $-$ step velocities to be $\sim 15:1$ for their boron oxyanion coprecipitation experiments. Assuming the borate species also to be incompatible, enrichment of boron should be favored in the faster moving $+$ steps for this explanation to be valid. However, they observed the opposite, with boron enrichment in the $-$ steps. Inasmuch as we also exhibit Cr enrichment in the slower moving $-$ steps, we conclude that this kinetic model does not explain the differential incorporation. Hence we conclude that structural differences between the nonequivalent growth steps and their influence on CrO_4^{2-} coordination at the steps are likely to be the primary factors controlling differential incorporation of oxyanions.

4.3. Overall partition coefficient trends

Our previous discussion has just demonstrated that Cr(VI) partitioning into calcite depends on the detailed configuration of surface steps. Consequently, at the interfacial scale, metal partitioning behavior cannot be represented simply by a single partition coefficient (K_d). Nevertheless, empirical K_d values remain useful for comparing the combined effects of multiple experimental factors on the overall partitioning behavior. For example, it is not uncommon to observe that the value of a partition coefficient is dependent on trace element concentration in solution as observed in our study. In calcium carbonate systems, such behavior has been described for strontium (Pingitore and Eastman, 1986), magnesium (Mucci and Morse, 1983) and boron oxyanion (Hemming et al., 1995) coprecipitation experiments with calcite. In all these studies, at relatively low fluid concentration of the trace element the partition coefficient decreases with increasing fluid concentration of the trace element, and achieves a nearly constant value at higher fluid concentration.

Mucci and Morse (1983) explained the decrease of K_d with increasing Mg solution concentration (strictly, the Mg:Ca ratio) as a preferential enrichment of Mg in the adsorbed layer on calcite at lower fluid Mg:Ca ratio (relative to higher Mg:Ca). They envisioned that the amount of Mg incorporated into the calcite, as expressed by the partition coefficient, reflected the composition in the adsorbed layer. Pingitore and Eastman (1986) described a similar behavior of the Sr^{2+} K_d with calcite as a deviation from Henry's law behavior, also referred to as the "Henry's law problem" (Navrotsky, 1978). One of the explanations proposed for the variation of the partition coefficient with concentration is incorporation of trace cations in more than one site. Pingitore and Eastman (1986) suggested that their observed partition coefficient behavior could be explained by the

preferential incorporation of Sr^{2+} impurities at minority sites with higher affinity for binding impurities than lattice sites. If the number of such sites in growing calcite is assumed to be small compared to the number of normal structural sites, the ratio of occupied minority sites to occupied structural sites is relatively high at low impurity concentrations, resulting in high K_d values. At higher impurity concentrations, this ratio is relatively small, and K_d^* values are more representative of Sr^{2+} incorporation into structural sites in calcite. Hemming et al. (1995) also suggested that preferential filling of such minority sites, which are limited in number, might explain boron coprecipitation systematics with calcite.

The preferential filling of such minority sites can be a possible explanation for our observations. At low CrO_4^{2-} concentration, the minority site contribution may be significant relative to that of the lattice sites, and as Cr solution concentration increases, the Cr occupying lattice sites eventually overwhelms Cr in the limited number of these minority sites.

No comparable effort was made to quantitatively examine the partitioning behavior of Cr into the calcite single crystals grown via the Gruzensky method. As we showed earlier, the Cr partitioning differs between the nonequivalent vicinal regions of the overgrowths as a result of specific preferences for the growth steps. Analyses of the (10 $\bar{1}$ 4) surface of a crystal grown with an initial solution Cr concentration of 60 mM showed Cr concentrations of 225 ppm in the + vicinals and 620 ppm in the - vicinals. Using Eq. (3) above, it is possible to calculate K_d^* values of 0.072 for the + vicinals and 0.199 for the - vicinals. However, it is important to note that these K_d^* values should not be directly compared to those for the constant-addition method. As we discussed, Eq. (3) is a simplification made by introducing a parameter, C, that represents the carbonate species in both the solid and the solution. Hence, only in experimental systems where the value of this parameter is the same can the calculated K_d^* values be compared. The carbonate speciation in the two growth solutions is different. Furthermore, in the Gruzensky method the solution was gradually depleted of Cr during growth, whereas for the constant-addition method near steady-state [Cr] and solution conditions prevailed. The K_d^* values for the Gruzensky system do not represent steady-state conditions, therefore we did not directly compare the K_d^* values from different Gruzensky experiments.

5. CONCLUSIONS

In this study, the systematic behavior and microscopic mechanisms of CrO_4^{2-} incorporation into calcite during crystal growth were studied. Batch experiments showed that $[\text{Cr}]_{\text{solid}}$ increases with increasing $[\text{Cr}]_{\text{solution}}$. Apparent partition coefficient values, K_d^* , are highest at low $[\text{Cr}]_{\text{solution}}$, and decrease to a constant value with increasing $[\text{Cr}]_{\text{solution}}$. A possible explanation for this behavior is the preferential filling of a limited number of minority sites with a high affinity for binding impurities. μ -XRF imaging shows that Cr is preferentially incorporated into the - steps of growth spirals on single crystal calcite (10 $\bar{1}$ 4) growth

surfaces. A satisfactory explanation for this surface site preference remains unclear; however, differences in the surface-site coordination geometry are believed to be important. XANES shows that Cr(VI) undergoes no reduction during incorporation. Furthermore, there is no reduction of Cr(VI) in the X-ray beam up to 2 days. EXAFS analysis confirms the incorporation of chromate into calcite structure, and shows that the incorporated Cr(VI) is coordinated by four oxygen atoms at a distance of ~ 1.64 Å, consistent with CrO_4^{2-} . Due to the low concentration of coprecipitated Cr and poor quality of the EXAFS data, best fits for higher shells are less certain. However, a likely fit shows that the second shell is split with ~ 2.3 Ca atoms at ~ 3.33 Å and ~ 2.1 Ca atoms at ~ 3.55 Å, which is consistent with substitution of CrO_4^{2-} in the carbonate sites.

This work is the first study of the microscopic and macroscopic behavior and mechanisms of hexavalent chromium coprecipitation with calcite. It provides a quantitative basis for understanding how structurally incompatible tetrahedrally coordinated oxyanions incorporate into calcite, from the view points of reactions occurring at the mineral-water interface, the structure of incorporated ions, and the path-dependent, surface site geometry-controlled incorporation of trace elements into calcite. The results suggest that interaction with calcite should not be overlooked when addressing the fate of CrO_4^{2-} in environments where calcite crystallization is possible. However, there are several factors that must be considered for application to real systems. In particular, the observation that partitioning of CrO_4^{2-} into calcite is dependent on the Cr solution concentration and on the type and availability of surface sites may limit quantitative applications. Nevertheless, this work provides a starting point for further investigations of CrO_4^{2-} behavior in calcium carbonate systems.

ACKNOWLEDGMENTS

This work was supported by the Center for Environmental Molecular Science through NSF Grant CHE-0221924. We thank A. Lanzirrotti (X26A, NSLS), K. Pandya (X11A, B, NSLS), N. Leyarovska (BESSRC, APS), and M. Balasubramanian (PNC-CAT, APS) for assistance with data collection. Comments from the associate editor Dr. Roy Wogelius and two anonymous reviewers greatly improved the manuscript.

REFERENCES

- Alexandratos V.G. (2004) Macroscopic and spectroscopic studies of arsenate uptake by calcite. M.Sc. thesis, State University of New York at Stony Brook.
- Allison J.D., Brown D.S., and Novo-Gradac K.J. (1990) MINT-EQA2/PRODEFA2—a geochemical assessment model for environmental systems—version 3.0 user's manual: Environmental Research Laboratory, Office of Research and Development, U.S. Environmental Protection Agency, Athens, Georgia, 106p.
- Beliles R. P. (1979) The lesser metals. In *Toxicity of Heavy Metals in the Environment. Part 2*, (ed. F.W. Oehme), pp. 547–616. M. Dekker, New York.

- Burns R. G. (1993) *Mineralogical Application of Crystal Field Theory*, 2nd ed. Cambridge University Press.
- Busenberg E., and Plummer L. N. (1985) Kinetic and thermodynamic factors controlling the distribution of SO_4^{2-} and Na^+ in calcite and aragonites. *Geochim. Cosmochim. Acta* **49**, 713–725.
- Dove P. M., and Hochella, Jr., M. F. (1993) Calcite precipitation mechanisms and inhibition by orthophosphate: in situ observations by scanning force microscopy. *Geochim. Cosmochim. Acta* **57**, 705–714.
- Elzinga E. J., and Reeder R. J. (2002) X-ray absorption spectroscopy study of Cu^{2+} and Zn^{2+} adsorption complexes at the calcite surface: implication for site-specific metal incorporation preferences during calcite crystal growth. *Geochim. Cosmochim. Acta* **66**, 3943–3954.
- Fendorf S. E. (1995) Surface reactions of chromium in soils and waters. *Geoderma* **67**, 55–71.
- Fendorf S., Eick M. J., Grossl P., and Sparks D. L. (1997) Arsenate and chromate retention mechanisms on goethite. 1. Surface structure. *Environ. Sci. Technol.* **31**, 315–320.
- García-Sánchez A., and Álvarez-Ayuso E. (2002) Sorption of Zn, Cd and Cr on calcite: application to purification of industrial wastewaters. *Miner. Eng.* **12**, 539–547.
- Garman S. M., Luxton T. P., and Eick M. J. (2004) Kinetics of chromate adsorption on goethite in the presence of sorbed silicic acid. *J. Environ. Qual.* **33**, 1703–1708.
- Gratz A. J., Hillner P. E., and Hansma P. K. (1993) Step dynamics and spiral growth on calcite. *Geochim. Cosmochim. Acta* **57**, 491–495.
- Gruzinsky P. M. (1967) Growth of calcite crystals. In *Crystal Growth*, (ed. H.S. Peiser), pp. 365–367. Pergamon Press.
- Hall P. O., and Aller R. C. (1992) Rapid, small-volume, flow injection analysis for CO_2 and NH_4^+ in marine and fresh waters. *Limnol. Oceanogr.* **37**, 1113–1119.
- Hemming N. G., Reeder R. J., and Hanson G. N. (1995) Mineral-fluid partitioning and isotopic fractionation of boron in synthetic calcium carbonate. *Geochim. Cosmochim. Acta* **59**, 371–379.
- Hemming N. G., Reeder R. J., and Hart S. R. (1998) Growth-step-selective incorporation of boron on the calcite surface. *Geochim. Cosmochim. Acta* **62**, 2915–2922.
- Hoffmann M. M., Darab J. G., and Fulton J. L. (2001) An infrared and X-ray absorption study of the equilibria and structures of chromate, bichromate, and dichromate in ambient aqueous solutions. *J. Phys. Chem. A* **105**, 1772–1782.
- Kendelewicz T., Liu P., Doyle C. S., Brown, Jr., G. E., Nelson E. J., and Chambers S. A. (1999) X-ray absorption and photoemission study of the adsorption of aqueous Cr(VI) on single crystal hematite and magnetite surfaces. *Surf. Sci.* **424**, 219–231.
- Lorence R. B. (1981) Sr, Cd, Mn and Co distribution coefficients in calcite as a function of calcite precipitation rate. *Geochim. Cosmochim. Acta* **45**, 553–561.
- Lu F. Q., Smith J. V., Sutton S. R., Rivers M. L., and Davis A. M. (1989) Synchrotron X-ray fluorescence analysis of rock-forming minerals. 1. comparison with other techniques; 2. white-beam energy-dispersive procedure for feldspars. *Chem. Geol.* **75**, 123–143.
- McIntire W. L. (1963) Trace element partition coefficients—a review of theory and applications to geology. *Geochim. Cosmochim. Acta* **27**, 1209–1264.
- Morse J. W., and Bender M. L. (1990) Partition coefficients in calcite: examination of factors influencing the validity of experimental results and their application to natural systems. *Chem. Geol.* **82**, 265–277.
- Mucci A., and Morse J. W. (1983) The incorporation of Mg^{2+} and Sr^{2+} into calcite overgrowths: influence of growth rate and solution composition. *Geochim. Cosmochim. Acta* **47**, 217–233.
- Navrotsky A. (1978) Thermodynamics of element partitioning: (1) systematics of transition metals in crystalline and molten silicates and (2) defect chemistry and the “Henry’s law problem”. *Geochim. Cosmochim. Acta* **42**, 887–902.
- Pandya K. I. (1994) Multiple-scattering effects in x-ray-absorption fine structure: chromium in a tetrahedral configuration. *Phys. Rev. B* **50**(21), 509–515.
- Paquette J., and Reeder R. J. (1990) New type of compositional zoning in calcite: insights into crystal-growth mechanisms. *Geology* **18**, 1244–1247.
- Paquette J., and Reeder R. J. (1995) Relationship between surface structure, growth mechanism, and trace element incorporation in calcite. *Geochim. Cosmochim. Acta* **59**, 735–749.
- Patterson R. R., Fendorf S., and Fendorf M. (1997) Reduction of hexavalent chromium by amorphous iron sulfide. *Environ. Sci. Technol.* **31**, 2039–2044.
- Palmer C. D., and Wittbrodt P. R. (1991) Processes affecting the remediation of chromium-contaminated sites. *Environ. Health Perspect.* **92**, 25–40.
- Parkhurst D.L., and Appelo C.A.J. (1999) User’s guide to PHREEQC (Version 2)—a computer program for speciation, batch-reaction, one-dimensional transport, and inverse geochemical calculations. U.S. Geol. Surv. Water Res. Inv. Rept. 99–4259, 310p.
- Peterson M. L., Brown, Jr., G. E., Parks G. A., and Stein C. L. (1997) Differential redox and sorption of Cr (III/VI) on natural silicate and oxide minerals: EXAFS and XANES results. *Geochim. Cosmochim. Acta* **61**, 3399–3412.
- Phillips B. L., Lee Y. J., and Reeder R. J. (2005) Organic coprecipitates with calcite: NMR spectroscopic evidence. *Environ. Sci. Technol.* **39**, 4533–4539.
- Pingitore, Jr., N. E., and Eastman M. P. (1986) The coprecipitation of Sr^{2+} with calcite at 25 °C and 1 atm. *Geochim. Cosmochim. Acta* **50**, 2185–2203.
- Reeder R. J., Lamble G. M., Lee J., and Staudt W. J. (1994) Mechanism of SeO_4^{2-} substitution in calcite: an XAFS study. *Geochim. Cosmochim. Acta* **58**, 5639–5646.
- Reeder R. J. (1996) Interaction of divalent cobalt, zinc, cadmium, and barium with the calcite surface during layer growth. *Geochim. Cosmochim. Acta* **60**, 1543–1552.
- Reeder R. J., Nugent M., Lamble G. M., Tait C. D., and Morris D. (2000) Uranyl incorporation into calcite and aragonite: XAFS and luminescence studies. *Environ. Sci. Technol.* **34**, 638–644.
- Ressler T. (1997) WinXAS: a new software package not only for the analysis of energy-dispersive XAS data. *J. Phys. IV* **7**, C2–C269.
- Sen S., Stebbins J. F., Hemming N. G., and Ghosh B. (1994) Coordination environments of boron impurities in calcite and aragonite polymorphs: an ^{11}B MAS NMR study. *Am. Mineral.* **79**, 818–825.
- Scott E. F. (1994) Surface reaction of chromium in soils and waters. *Geoderma* **67**, 55–71.
- Shannon R. D. (1976) Revised effective ionic radii and systematic studies of interatomic distances in halides and chalcogenides. *Acta Crystallogr.* **A32**, 751–767.
- Staudt W. J., Reeder R. J., and Schoonen M. A. A. (1994) Surface structural controls on compositional zoning of SO_4^{2-} and SeO_4^{2-} in synthetic calcite single crystals. *Geochim. Cosmochim. Acta* **58**, 2087–2098.
- Szulcowski M. D., Helmke P. A., and Bleam W. F. (1997) Comparison of XANES analyses and extractions to determine chromium speciation in contaminated soils. *Environ. Sci. Technol.* **31**, 2954–2959.
- Temmam M., Paquette J., and Vali H. (2000) Mn and Zn incorporation into calcite as a function of chloride aqueous concentration. *Geochim. Cosmochim. Acta* **64**, 2417–2430.

- Teng H. H., Dove P. M., Orme C. A., and De Yoreo J. J. (1998) Thermodynamics of calcite growth: baseline for understanding biomineral formation. *Science* **282**, 724–727.
- Teng H. H., Dove P. M., and De Yoreo J. J. (2000) Kinetics of calcite growth: Surface processes and relationships to macroscopic rate laws. *Geochim. Cosmochim. Acta* **64**, 2255–2266.
- Tesoriero A. J., and Pankow J. F. (1996) Solid solution partitioning of Sr^{2+} , Ba^{2+} , and Cd^{2+} to calcite. *Geochim. Cosmochim. Acta* **60**, 1053–1063.
- Weckhuysen B. M., Wachs I. E., and Schoonheydt R. A. (1996) Surface chemistry and spectroscopy of chromium in inorganic oxides. *Chem. Rev.* **96**, 3327–3349.
- Wei Y., Chiu S., Tsai H., Yang Y., and Lee J. (2002) Thermal stabilization of chromium(VI) in kaolin. *Environ. Sci. Technol.* **36**, 4633–4641.
- Zabinsky S. I., Rehr J. J., Ankudinov A., Albers R. C., and Eller M. J. (1995) Multiple-scattering calculations of X-ray absorption spectra. *Phys. Rev.* **B52**, 2995–3009.
- Zachara J. M., Ainsworth C. C., Cowan C. E., and Resch C. T. (1989) Adsorption of chromate by subsurface soil horizons. *Soil Sci. Soc. Am. J.* **53**, 4148–4428.
- Zachara J. M., Ainsworth C. C., Brown, Jr., G. E., Catalano J. G., Mckinley J. P., Qafoku O., Smith S. C., Szecsody J. E., Traina S. J., and Warner J. A. (2004) Chromium speciation and mobility in a high level nuclear waste vadose zone plume. *Geochim. Cosmochim. Acta* **68**, 13–30.
- Zhong S., and Mucci A. (1992) Calcite precipitation in seawater using a constant addition technique: a new overall reaction kinetic expression. *Geochim. Cosmochim. Acta* **57**, 1409–1417.

Associate editor: Roy A. Wogelius